A Comparative Study of Defect States in Evaporated and Selenized CIGS(S) Solar Cells

P.K. Johnson[1†], J.T. Heath[2*], J.D. Cohen[2], K.Ramanathan[3], and J.R. Sites[1]

1. Department of Physics, Colorado State University, Fort Collins, CO 80525, U.S.A.
2. Department of Physics, University of Oregon, Eugene, OR 97403, U.S.A.
3. National Renewable Energy Laboratory, 1617 Cole Blvd., Golden, CO 80401, U.S.A.

[†]Corresponding author: p_johnson@energymail.com (303) 939-6757 (970) 491-7947 (fax)
Present address: Ball Aerospace & Technologies Corp., 1600 Commerce St., Boulder CO 80301, U.S.A.

*Present address: Department of Physics, Linfield College, McMinnville, OR 97218, U.S.A.

Keywords: CIGS(S), Solar cells, Defects, Carrier density, AS, DLCP, Polycrystalline, Cd PE

ABSTRACT

Current-voltage, admittance spectroscopy, and drive-level capacitance profiling measurements were taken on $Cu(In_{1-x}Ga_x)(Se_{1-y}S_y)_2$ solar-cell devices. The devices were made using two different types of absorbers. One set of absorbers was deposited via physical vapor deposition, while the other set of absorbers was made by selenization of metal precursors. Additionally, each type of absorber was completed with one of two different types of buffer treatments: a CdS layer or a cadmium partial electrolyte surface modification. The devices with the evaporated absorbers had larger values of V_{OC}, higher carrier densities, lower densities of trapping defects, and likely shallower gap states. Results were qualitatively similar for the CdS and partial electrolyte buffers.

INTRODUCTION

Thin-film solar cells made with two different processes for the deposition of $Cu(In_{1-x}Ga_x)Se_2$ (CIGS) or $Cu(In_{1-x}Ga_x)(Se_{1-y}S_y)_2$ (CIGSS) absorbers were studied using current-voltage (J-V), quantum efficiency (QE), admittance spectroscopy (AS), and drive-level capacitance profiling (DLCP) measurement techniques in an attempt to correlate spatial defect profiles with solar-cell performance. One set of absorbers was deposited using physical vapor deposition and the other set of absorbers was prepared by selenization of metal precursor films. The absorbers deposited by physical vapor deposition were prepared using the patented three-stage process at the National Renewable Energy Laboratory (NREL) and will be referred to as "evaporated" [1-2]. The absorbers prepared by selenization were grown at Siemens (now Shell) Solar Industries (SSI) in Camarillo, California and will be referred to as "selenized" [3,4].

Currently the highest efficiency laboratory CIGS cells come from the three-stage evaporation process, whereas the highest efficiency large-area CIGS(S) modules are made using selenization of the metallic elements. The motivation for making devices that differ only in their absorbers is to correlate device performance with quantifiable electronic-state differences between the two types of devices. The evaporated absorbers are CIGS, while the selenized absorbers also contain sulfur and will be referred to as CIGSS. Some reports have suggested that incorporation of sulfur may passivate defects [5-7], but we did not find evidence for reduced defects in the sulfur-containing cells. For the results reported here, the difference in deposition processes appears to play a more significant role than the partial substitution of selenium by sulfur.

In addition to absorber differences, two types of buffer treatments were compared. The junctions in several devices of each absorber type were formed using a standard chemical-bath deposition (CBD) resulting in a CdS buffer layer, while other nominally identical absorbers were treated in a sulfur-free bath to prepare a non-CdS junction. The latter process, referred to as the cadmium partial electrolyte (Cd PE), modifies the absorber surface, but does not result in a separate device layer [8,9]. The original motivation was to explore Cd PE as an alternative buffer layer process to CdS deposition and thus better understand junction formation and the role of Cd in the CIGS surface layer [8]. However, Cd PE devices are also of interest because their high band-gap window layer improves the current of the device and because the Cd PE process produces less waste than the typical CBD-CdS process. All devices were then completed with depositions of an i-ZnO layer, an n-ZnO layer, and Ni/Al grids for contact. The resulting sample set consisted of the four different types of devices from combinations of the two types of absorbers and the two junction-preparation techniques.

RESULTS

Prior to temperature-dependent capacitance measurements including AS and DLCP, comparative J-V and QE measurements were made, primarily at room temperature. The illuminated J-V curves from representative cells selected from each of the four fabrication modes are shown in Figure 1a, and the corresponding QE curves are shown in Figure 1b. The cell parameters deduced from the J-V measurements, as well as

the band gaps deduced from the long-wavelength cutoff of the QE curves, are listed in Table I.

For devices made with a common buffer layer, CdS or Cd PE, the evaporated absorbers had consistently higher V_{OC} values and consistently higher band gaps than the selenized cells. The band-gap difference between evaporated and selenized devices was about 70 meV. Even after adjustment for this difference, the evaporated devices with each buffer type had larger V_{OC} values than the selenized devices made with the same buffer. As shown in both Figure 1 and Table I, the evaporated devices also had a higher fill factor (FF). This is due in part to a slightly lower diode quality factor, A, which often correlates with higher voltage. Also apparent from both Figure 1 and Table I is the larger short-circuit current density J_{SC} of the Cd PE devices (triangles in the figure), primarily due to improved current collection at wavelengths less than 520 nm.

Admittance spectroscopy (AS) measurements, i.e. capacitance and conductance vs. frequency at multiple temperatures, were taken on the four types of samples. There was no dc bias applied during these measurements, and the data were gathered at temperatures ranging between 100 and 300 K. The majority of the AS measurements were taken at the University of Oregon using an SRS 850 lock-in amplifier and SRS 570 current to voltage preamplifier. However, two of the samples were measured at Colorado State University using an HP 4192A LF impedance analyzer. The results from the two instruments were entirely consistent. More details on AS can be found in the literature [10-14]. Representative scans of capacitance per unit area (C/A) versus frequency f for each of the four device types are shown in Figures 2 and 3. The AS data (Fig. 2) from the evaporated cells shows very little variation as a function of frequency, while that from the selenized cells (Fig. 3) shows a much larger difference between high and low frequencies. All curves had significant noise at the lowest frequencies.

A downward step in a capacitance versus frequency isotherm is indicative of a transition from a frequency-temperature region where a defect responds (i.e. where it traps and releases carriers at a rate greater than the measurement frequency) to a region where the same defect is not able to respond to the applied frequency. The broader transitions seen in this work are indicative of a range of defect energies.

Defect levels can affect the solar cells in at least two ways: shallower levels can improve device performance by contributing carriers at room temperature, while deeper levels can detract from device performance by enhancing recombination. We assume a fairly simple model in which the high-frequency capacitance reflects the response of the free carrier density, while the low-frequency capacitance reflects the sum of the carrier plus trap densities [15]. The evaporated devices in Figure 2 showed small, yet measurable, changes in capacitance with frequency, indicative of a small density of defects acting as hole traps, while the selenized devices in Figure 3 exhibited significant frequency-dependence of the capacitance, indicative of a large density of hole traps. Measurements on similar devices yielded roughly the same results.

Figures 2 and 3 also show the difference between the values of the high frequency capacitance/area (C/A) for the evaporated and selenized devices. Assuming that there is no significant charge density at the interface, and the absorbers are reasonably uniform spatially, the evaporated devices (Figure 2) indicate an approximate free carrier (hole) density in the low-10^{15} cm^{-3} range, while the selenized devices have high frequency C/A values that lead to an approximate free carrier (hole) density mostly in the mid-10^{14} cm^{-3} range. Thus, AS suggests that there are more free carriers, as well as fewer trapping defects in the evaporated devices. The approximate free-carrier and trapping densities are summarized in Table II.

The Table II estimates employ the numerical-analysis methods described in Ref. [16] assuming a defect energy distributed uniformly throughout the depletion region. Uncertainties in its energy and the value of built-in potential lead to a factor-of-two uncertainty in values for free-carrier and defect densities. Other modeling parameters such as the valence-band effective density of states, thermal emission prefactor, and width of the defect band have little effect on the Table II estimates.

Defining f_i as the frequency at which the capacitance is half way between our best estimates of the high- and low-frequency limits for each AS curve, and using the measurement temperature for each curve, we calculated an average thermal activation energy E_a for the detected defects from the relationship [12-14]

$$2\pi f_i/T^2 = \nu_o \exp(-E_a/k_B T), \qquad (1)$$

where $\nu_o = \sigma_p v_{th} N_v / T^2$. The individual factors (hole cross section σ_p, thermal velocity v_{th}, and the effective density of states in the valence band N_v) are not independently determined and are not critical for these results. When there is one well-defined activation energy E_a for the defect response, one usually identifies this as the approximate energy difference between the valence band edge and the available energy state in the band gap created by the defect. A band of defects covering a small range of energies within the gap will exhibit an average value for E_a determined in this fashion. A larger value of E_a generally indicates a slower hole release rate and hence a higher likelihood that the detected defect(s) may act as a recombination center(s).

A graph displaying the activation energies and the prefactors υ_o of the defects detected by device type is shown in Figure 4. Four of these E_a values were deduced from the data shown in Figures 2 and 3, and the others from data on similar cells. The defect response detected in the selenized devices occurred at activation energies ranging from 150 to 250 meV, while the defects detected in the evaporated devices had much smaller activation energies, ranging from 40 to 75 meV. Thus, the defects detected in the evaporated devices have faster carrier-release rates and are less likely to be involved in recombination. Moreover, they are more likely to be ionized at room temperature and hence provide additional hole carriers to the device.

The drive-level capacitance profiling (DLCP) technique [16,17] was employed to profile the defect density as a function of distance from the materials interface of the CIGS(S) and the adjoining buffer/window layer. DLCP actually determines the depletion region charge density in the vicinity of the location x_e, where this is defined as the location at which $E_F - E_v = E_e$. Here E_F is the (quasi) Fermi energy, E_v the energy of the valence band edge, and E_e the energy at which the occupation of a gap state can change just rapidly enough to follow the applied alternating bias at frequency f [16]:

$$E_e \equiv k_B T \ln(\nu_o T^2 / 2\pi f), \qquad (2)$$

which is of the same form as Eqn. (1) for the activation energy.

In the special case of one single dominant defect, located at energy E_e from the valence band edge and with trapping density much greater than the free carrier density, x_e is the spatial location at which the defect level crosses the quasi Fermi level. In the DLCP technique, the position of x_e within the sample is varied by adjusting the dc bias

and the density of carriers responding at the position x_e is determined by analyzing the change in capacitance when the oscillating voltage amplitude is changed. The DLCP signal shows the sum of all states that can respond dynamically to the ac perturbation, including both the free carriers and deeper trapping states in the lower frequency (or higher temperature) regime. However, at sufficiently low temperatures it is assumed trapping defect states within the band gap cannot respond, and hence the DLCP response is due solely to the free carrier contribution detected near the edge of the depletion region. Thus, as temperature is decreased, the DLCP density will approach a limiting value that indicates the free carrier density in the p-type absorber. At higher temperatures, the trapping defect states also respond. It is assumed that the *difference* between the maximum and minimum limiting responses at the high and low end of the temperature range of the measurement corresponds to the density of the dominant responding traps, N_t. The detected states will generally not be interface states. In order for an interface state to contribute to the DLCP response, the defect energy E_e and the quasi Fermi energy at the interface would need to coincide. In the unlikely case an interface state does contribute to DLCP, it would give a distinctive response as the DC bias is varied [16].

Typical DLCP data for both types of selenized cell are displayed in Figure 5. Fig. 5a are the results from a CdS-buffer cell, and Fig. 5b from a Cd PE cell. They clearly show the limiting high and low temperature responses and can hence be used to estimate the free carrier density p and the density of trapping-state defects N_t. The sum of N_t and p, labeled $N_{DL\,max}$ in Figure 5, is the high-temperature limiting value of the measurement. In Figure 5 the horizontal axis is $\langle x \rangle = \frac{\varepsilon A}{C_o}$, where C_o is the capacitance value obtained for the lowest amplitude ac voltage limit obtained at a particular nominal dc bias [16]. It is important to note that <x> is the average spatial location of the ac charge response in the device, and thus it reflects *all* the responding states -- the free carriers at the edge of the depletion region and the response at x_e. Consequently, the positions given by <x> will typically be intermediate between the defect state(s) responding near x_e, and the depletion region edge.

The DLCP results for the two selenized devices exhibit a significant difference in defect response as a function of temperature. A measurement frequency of 11 kHz was chosen, because it was high enough to provide us good signal-to noise, and it also allowed us to observe the full defect response above 250 K, but only the carrier response below 160 K. Thus, at this frequency, the convenient 150-300 K temperature range allowed DLCP to span the full range of the possible defect response. From the data plotted in Figure 5, we deduce a free carrier density in the mid-10^{14} cm^{-3} range for both types of selenized devices, a trap density of approximately 6 x 10^{15} cm^{-3} for the selenized CdS device, but a slightly lower trap density (of approximately 3 x 10^{15} cm^{-3}) for the selenized Cd PE device. These DLCP trends and values are consistent with the results from AS: the large capacitance step in Figure 3a, and the somewhat smaller capacitance step in Figure 3b. The relatively low voltage of the selenized cells is likely the result of the higher defect density and lower carrier density.

The evaporated samples were not conducive to the DLCP analysis shown in Figure 5, because their response showed a steep spatial variation in state density and little variation with temperature. The lack of significant variation of defect response with temperature is consistent with the minimal defect response of AS measurements taken in the same temperature range. Although there was no clear low-temperature limit exhibited by the DLCP data, the lack of temperature variation of the DLCP data, together with the small step in the AS data, indicate that the density of trapping defects affecting these devices is very low. Indeed, the average estimated trap density of these two devices from the AS data was 5 x 10^{14} cm^{-3}, nearly an order of magnitude below the selenized devices.

DISCUSSION

The results from AS and DLCP measurements described above provide a number of potential reasons for the differences in the performance between the evaporated and selenized devices. First, the significantly lower defect densities in the evaporated devices is likely a primary reason why the evaporated devices have higher V_{OC} values than their selenized counterparts. Indeed, that is consistent with the correlation seen by other groups working on CISS [18]. However, our observations of large defect densities in the

selenized CIGSS cells studied are not consistent with reports [5-7] of significant sulfur passivation of defects in cells made elsewhere.

Secondary-Ion Mass Spectrometry (SIMS) measurements of CIGSS devices similar to those used in this study show two specific regions where the sulfur is concentrated, near the very front of the device and near the back of the device [19]. Thus, the lack of observed sulfur passivation in DLCP could be explained if the front region of sulfur concentration occurred closer to the cell interface than x_e, the closest distance that DLCP probes. A lower defect density near the interface, however, should affect the raw values of capacitance, and hence show up as a discrepancy between defect densities predicted by AS results and those measured with DLCP. Since the DLCP and AS results for this study are otherwise consistent, we conclude that the sulfur is not a primary factor.

The second significant difference noted between the evaporated and selenized devices is the larger activation energies of the defect response for the latter. In particular the AS results show that holes trapped in the defect band are released at a faster rate for the evaporated *vs.* selenized absorbers, thus making it less likely that such defects will facilitate recombination. In addition, the shallow activation energies exhibited by the evaporated samples (less than 0.1 eV) suggest that a larger portion of this acceptor band is ionized at room temperature, thus contributing to a higher carrier density in the evaporated devices and an effective trapping state density that is even less than the 3 x 10^{14} cm^{-3} estimated from AS, since those measurements were made at or below 220K.

CONCLUSIONS

This study of the defect properties of CIGS(S) has revealed significant differences in the electronic properties of selenized compared to evaporated absorbers. These differences may help explain corresponding differences in cell performance. Through QE, J-V and AS measurements, we have seen that the evaporated-absorber solar cells produce larger voltages relative to the band gap, have larger fill factors, smaller trapping state densities, lower defect activation energies, and larger hole carrier densities than those fabricated by selenization. Through DLCP, we have confirmed that the trapping state densities of the selenized devices are above 10^{15} cm^{-3}, similar to results from AS

measurements, and significantly larger than for the evaporated cells. The defect differences between the CdS and the partial electrolyte buffers were relatively modest, but those with the CdS buffers were somewhat larger. The quantitative evidence is strongly suggestive that the larger values of V_{OC} in the evaporated-absorber solar cells are a result of not only the larger estimated free carrier density, but also the smaller trapping state densities and the lower defect activation energies.

ACKNOWLEDGEMENTS

The authors would like to thank Dale Tarrant of SSI for providing the selenized absorbers used in this study and James Keane for cell completion. We are appreciative of funding through NREL Subcontracts ADJ-1-30630-06 (Colorado State) and XAD-9-18668-15 (Oregon).

REFERENCES

1. Contreras M, *et al*. High efficiency Cu(In,Ga)Se_2-based solar cells: Processing of novel absorber structures, *Proceedings of 24th IEEE Photovoltaics Specialists Conference* 1994; 68-75.
2. Gabor A, *et al*. High-efficiency $CuIn_xGa_{1-x}Se_2$ solar cells made from $(In_x,Ga_{1-x})_2Se_3$ precursor films, *Applied Physics Letters* 1994: **65**; 198-200.
3. Tarrant D, Ermer J, I-III-V Multinary Solar Cells Based on $CuInSe_2$, *Proceedings of 23rd IEEE Photovoltaics Specialists Conference* 1993; 372-378.
4. Shafarman W, Stolt L, in *Handbook of Photovoltaic Science and Engineering*, (A. Luque and S. Hegedus eds.), John Wiley and Sons, Chichester UK, 2003; 583.
5. Rau U, *et al*. Impact of Na and S incorporation on the electronic transport mechanisms of Cu(In,Ga)Se_2 solar cells, *Solid State Communications* 1998: **107**; 59-63.
6. Schock H, *et al*. High efficiency, high voltage solar cells by band gap and defect engineering in Cu(In,Ga)$(S,Se)_2$ chalcopyrite semiconductors, *Proceedings of 16th European Photovoltaic Solar Energy Conference* 2000; 304-308.
7. Jasenek A, Rau U, Nadenau V, Schock H, Electronic properties of $CuGaSe_2$-based heterojunction solar cells. Part II. Defect spectroscopy, *Journal of Applied Physics* 2000: **87**; 594-602.

8. Ramanathan K, *et al*. High efficiency $Cu(In,Ga)Se_2$ thin film solar cells without intermediate buffer layers, *Proceedings of 2nd World Photovoltaic Solar Energy Conference* 1998; 477-481.
9. Ramanathan K, *et al*. Properties of Cd and Zn partial electrolyte treated CIGS solar cells, *Proceedings of 29th IEEE Photovoltaics Specialists Conference* 2002; 523 -526.
10. Losee D, Admittance spectroscopy of impurity levels in Schottky barriers, *Journal of Applied Physics* 1975: **46**; 2204-2214.
11. Walter T, Herberholz R, Müller C, Schock H, Determination of defect distributions from admittance measurements and application to $Cu(In,Ga)Se_2$ based heterojunctions, *Journal of Applied Physics* 1996: **80**; 4411-4420.
12. Schmitt M, Rau U, Parisi J, Investigation of deep trap levels in $CuInSe_2$ solar cells by temperature dependent admittance measurements, *Proceedings of 13th European Photovoltaic Solar Energy Conference* 1995; 1969-1972.
13. Cohen D, Density of states from junction measurements, in *Semiconductors and Semimetals vol. 21C: Hydrogenated Amorphous Silicon*, ed. by J.I. Pankove (Academic, New York, 1984), pp. 9-98.
14. Pautrat J, *et al*. Admittance spectroscopy: A powerful characterization technique for semiconductor crystals--application to ZnTe, *Solid-State Electronics* 1980: **23**; 1159-1169.
15. Kimerling L, Influence of deep traps on the measurement of free-carrier distributions in semiconductors by junction capacitance techniques, *Journal of Applied Physics* 1974: **45**; 1839-1845.
16. Heath J, Cohen D, Shafarman W, The study of bulk and metastable defects in copper indium gallium diselenide thin films using drive-level capacitance profiling, *Journal of Applied Physics* 2004: **95**; 1000-1010.
17. Michelson C, Gelatos A, Cohen D, Drive-level capacitance profiling: Its application to determining gap state densities in hydrogenated silicon films, *Applied Physics Letters* 1985: **47**; 412-414.
18. Turcu M, Kötschau I, Rau U, Composition dependence of defect energies and band alignments in the $Cu(In_{1-x}Ga_x)(Se_{1-y}S_y)_2$ alloy system, *Journal of Applied Physics* 2002: **91**; 1391-1399.
19. Rockett A, private communication, 2001.

FIGURES

Figure 1. Current density *vs.* voltage (a) and quantum-efficiency (b) curves for representative cells of each type.

Figure 2. Admittance spectroscopy results for an evaporated, CdS device (a), and an evaporated, Cd PE device (b). Different symbols represent different measurement temperatures. Measurements were taken at 20 K intervals at zero applied bias.

Figure 3. Admittance spectroscopy results for a selenized, CdS device (a), and a selenized, Cd PE device (b). Different symbols represent different measurement temperatures. Measurements were taken at 20 K intervals at zero applied bias.

Figure 4. Activation energy and temperature-adjusted thermal emission prefactor of defects from AS studies. The values of E_a and υ_0 are notably larger for the selenized devices (filled symbols) than for the evaporated devices (open symbols).

Figure 5. Drive-level response of a selenized CdS device (a) and a selenized Cd PE device (b). These devices show high- and low-temperature saturation, which allows the trap state density N_t and the free carrier density p to be extracted. The measurement frequency was 11 kHz and the dc bias range was 0 to –1 V.

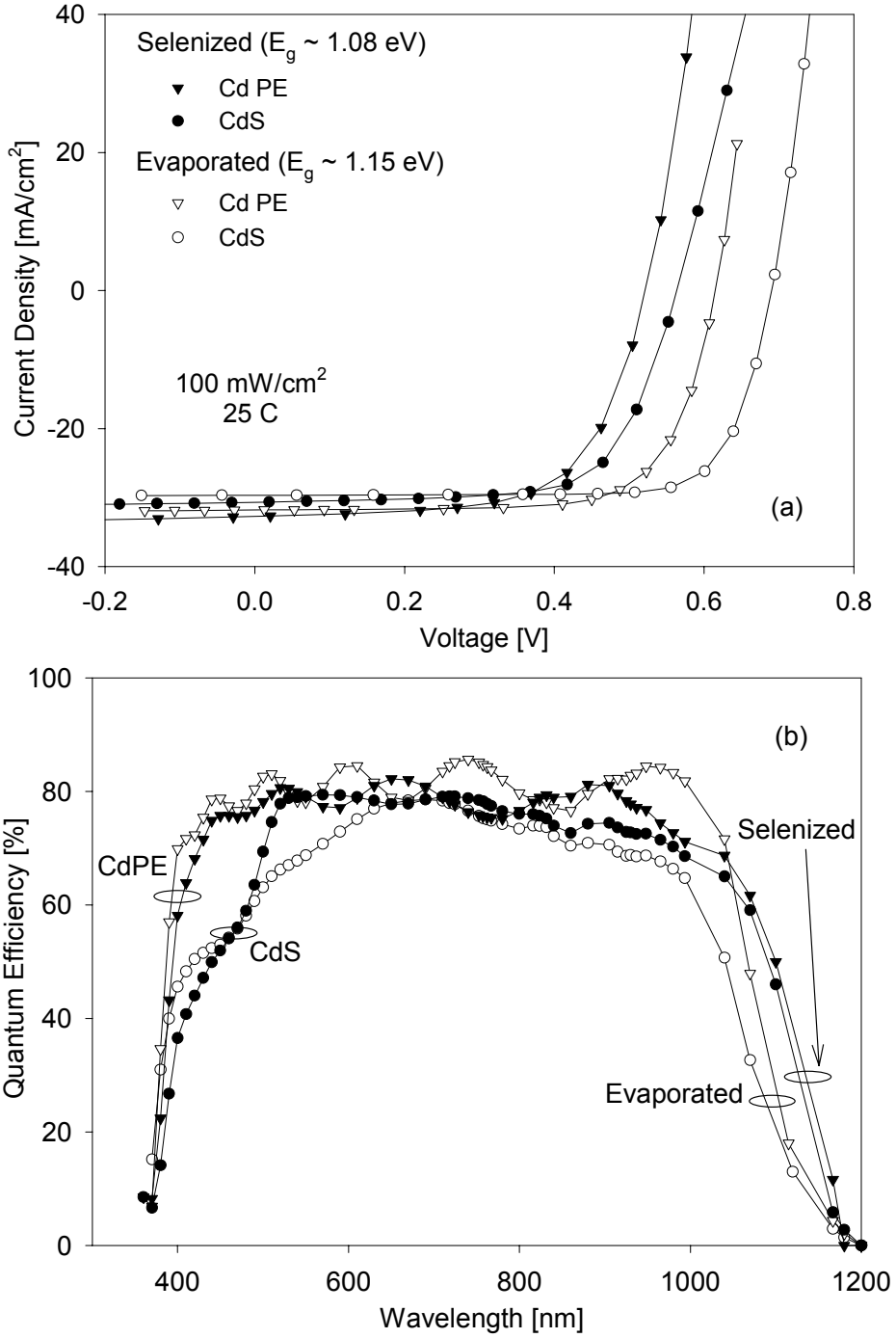

P. K. Johnson, et al., Figure 1

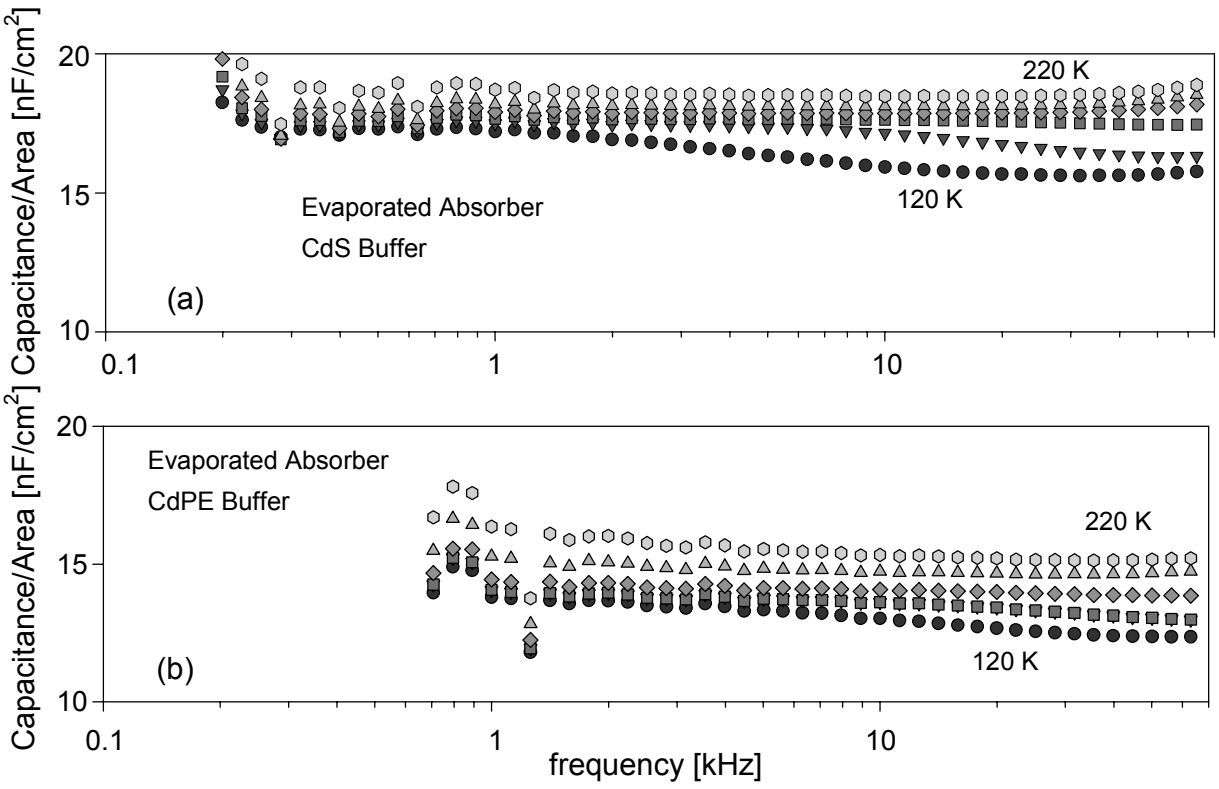

P. K. Johnson, et al., Figure 2

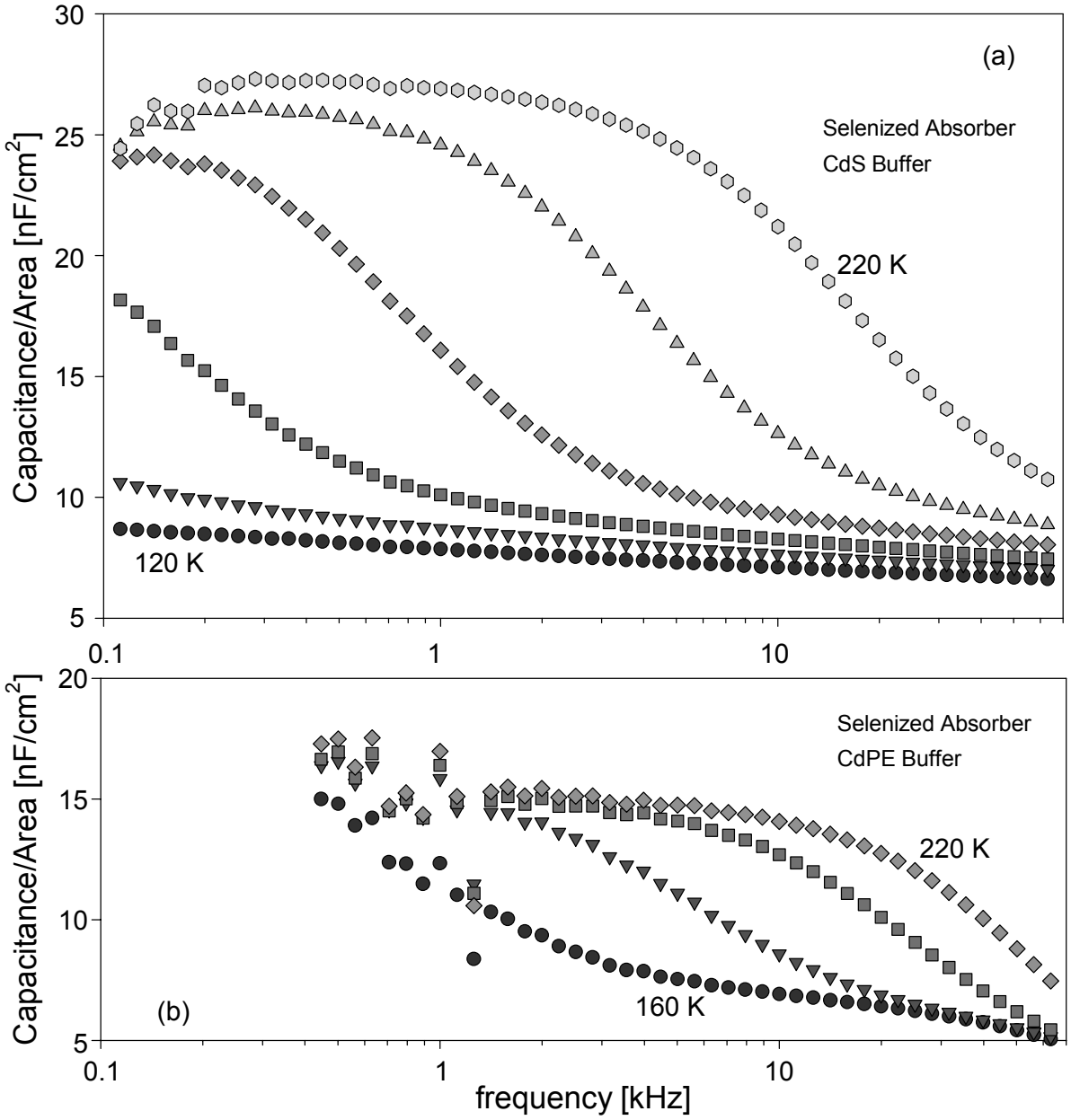

P. K. Johnson, et al., Figure 3

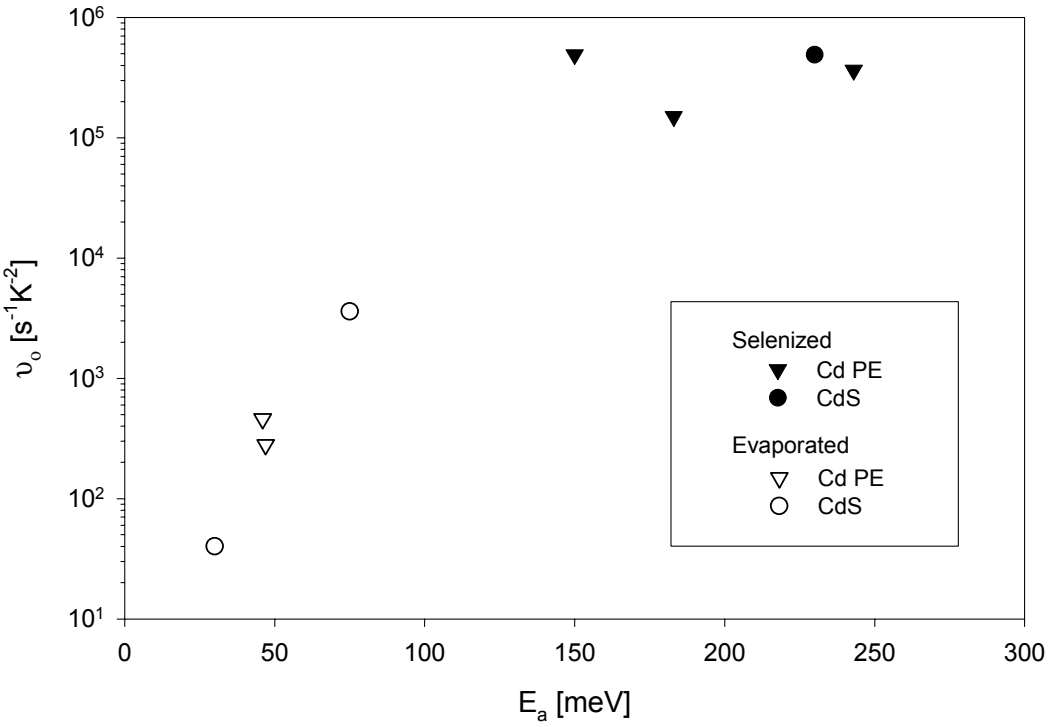

P. K. Johnson, et al., Figure 4

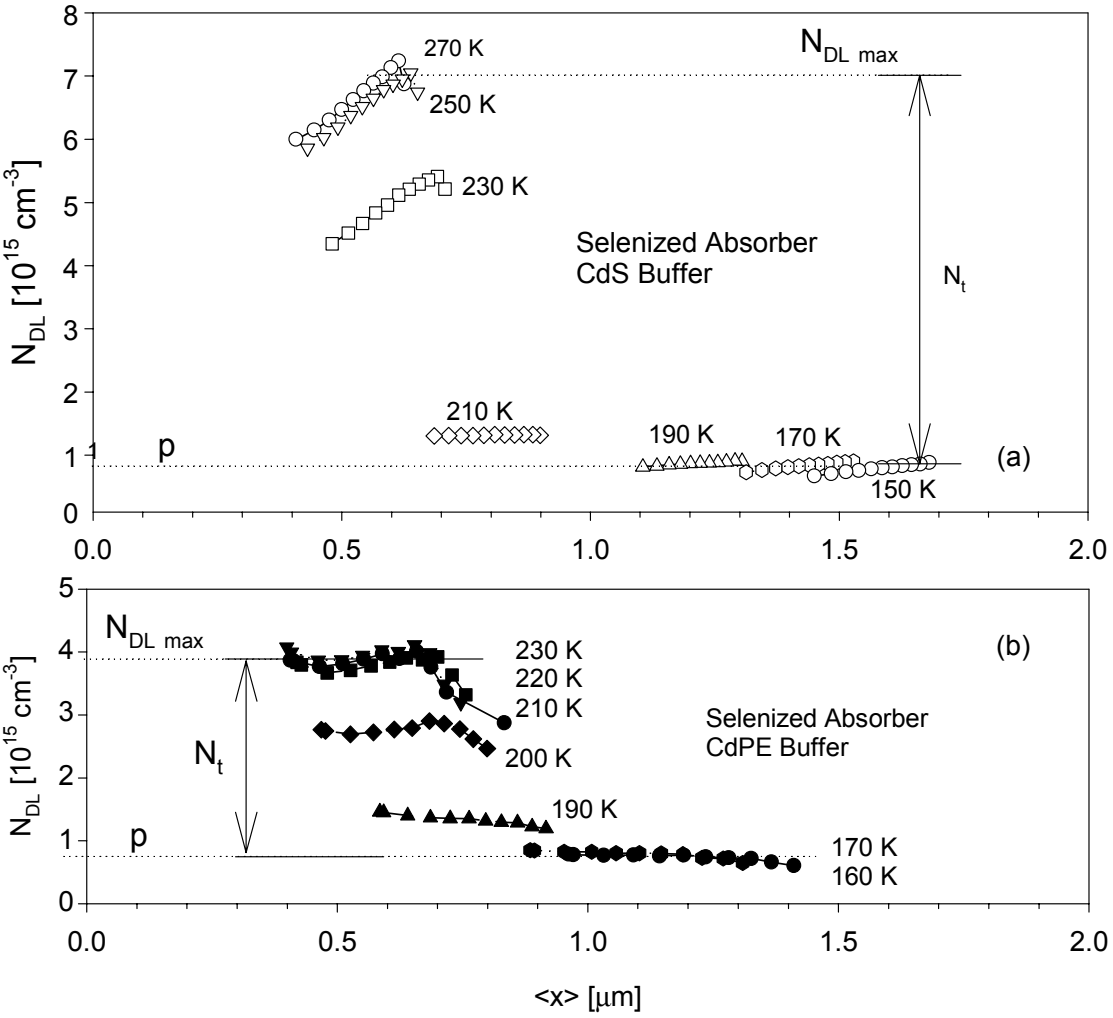

P. K. Johnson, et al., Figure 5

Device	V_{OC} (V)	E_g (eV)	$V_{OC} + \Delta E_g/q$ (V)	J_{SC} (mA/cm^2)	FF (%)	A
Selenized Cd PE	0.521	1.07	0.597	32.8	65.0	2.3
Selenized CdS	0.564	1.08	0.633	30.7	68.8	~2
Evaporated Cd PE	0.615	1.14	0.622	31.8	72.3	2.0
Evaporated CdS	0.690	1.15	0.690	29.7	78.3	1.5

TABLE I. Summary of illuminated J-V results and band gap deduced from room temperature QE measurement. J-V measurements were taken under standard illumination (100 mW/cm^2) at room temperature. $\Delta E_g = 1.15$ eV - E_g.

Device	Estimated Free Carrier Density from AS (cm^{-3})	Estimated Free Carrier Density from DLCP (cm^{-3})	Estimated Trapping State Density from AS (cm^{-3})	Estimated Trapping State Density from DLCP (cm^{-3})
Evaporated CdS	low 10^{15}	Not accessible	mid 10^{14}	Not accessible
Evaporated Cd	low 10^{15}	Not accessible	mid 10^{14}	Not accessible
Selenized CdS	mid 10^{14}	mid-high 10^{14}	mid 10^{15}	6 x 10^{15}
Selenized Cd PE	mid 10^{14}	mid-high 10^{14}	low 10^{15}	3 x 10^{15}

TABLE II. Semi-quantitative summary of results from AS and DLCP.